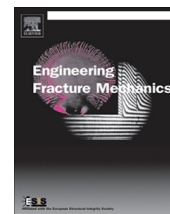


Contents lists available at [SciVerse ScienceDirect](#)

Engineering Fracture Mechanics

journal homepage: www.elsevier.com/locate/engfracmech

Microplane model M7f for fiber reinforced concrete



Ferhun C. Caner^{a,1}, Zdeněk P. Bažant^{b,*}, Roman Wendner^{b,3}

^a Institute of Energy Technologies, Technical University of Catalonia, Av. Diagonal No. 647, 08028 Barcelona, Spain

^b Department of Civil and Environmental Engineering, Northwestern University, 2145 Sheridan Road, Evanston, IL 60208, United States

ARTICLE INFO

Article history:

Received 26 December 2012

Received in revised form 25 March 2013

Accepted 27 March 2013

Available online 6 April 2013

Keywords:

Constitutive modeling

Fiber reinforced concrete

Inelastic behavior

Cracking damage

Fracture

Softening

Numerical algorithm

Thermodynamic potentials

Unloading

Cyclic loading

ABSTRACT

Model M7f is a new model for fiber reinforced concretes under static and dynamic loads, which features two kinds of improvement over the earlier versions: (1) It is built on M7, a new, greatly improved, microplane model for plain concrete; and (2) it includes a more realistic description of the fiber pullout and breakage. The former include: (a) the absence of volumetric deviatoric split of elastic strains, which eliminates excessive lateral expansions or contractions and stress locking in far post-peak extensions; (b) simulation of the differences between hydrostatic compression and uniaxial compression under rigid lateral confinement; and (c) high shear dilatancy of low strength concretes; and realistic description of unloading, reloading and load cycles, even if they cross between tension and compression. The latter includes an improved continuous dependence of the effect of fibers on the fiber volume fraction. The fiber resistance is a function of the strain representing the average opening of cracks of given spacing and, as in model M5f, a horizontal plateau as a function of the type of fiber and fiber volume fraction has been employed and used systematically for all fits. In this study, this horizontal plateau is justified using uniformly distributed crack bridging fibers. The model behavior is calibrated and verified by fitting of the main test data from the literature. The match of experimental observations and the computational results is closer than in the previous models.

© 2013 Elsevier Ltd. All rights reserved.

1. Introduction

The microplane models, which range from M0 to M7 and were developed since 1984 primarily for the constitutive behavior of concrete, are hierarchical semi-multiscale models [2], because the angular interactions of inelastic phenomena are captured explicitly whereas the interactions at a distance cannot be captured as a result of lumping the inelastic phenomena from a representative volume element into a single material point. In regard to softening damage, the hierarchical fully multiscale models for quasibrittle fracture are no better than the microplane models [2] because both miss the microcrack interactions that lead to localization of damage and fail to predict the size of the fracture process zone. The localization limiter, can be predicted only by numerical simulation of the microstructure, e.g., by a lattice-particle model, and must be externally imposed on both types of models.

* Corresponding author.

E-mail addresses: ferhun.caner@upc.edu (F.C. Caner), z-bazant@northwestern.edu (Z.P. Bažant), roman.wendner@boku.ac.at (R. Wendner).

¹ Associate Professor visiting Dept. of Civil and Environmental Engineering, Northwestern University.

² Distinguished McCormick Institute Professor and W.P. Murphy Professor of Civil Engineering, Mechanical Engineering and Materials Science.

³ Visiting Scholar on leave from BOKU Vienna.

Nomenclature

n_i	components of microplane unit vector
m_i	components of M -direction in-plane unit vector
l_i	components of L -direction in-plane unit vector
$c_1 \cdots c_{20}$	fixed material parameters of the model for concrete matrix
f'_c	compressive strength of concrete matrix
f'_{c0}	reference value of compressive strength of concrete matrix
$k_1 \cdots k_5$	free material parameters of the model for concrete matrix
$p_0 \cdots p_4$	fiber law material parameters
E	elastic modulus
E_0	reference value of the elastic modulus of the concrete matrix
G	shear modulus of elasticity of the model
K	bulk elastic modulus of the model M7f
\tilde{K}	bulk elastic modulus of the homogenous coupling material with zero shear modulus
\bar{K}	bulk elastic modulus of the parallel coupling model
E_N	microplane elastic normal modulus
E_{N0}	initial value of elastic normal modulus of (virgin) concrete
E_T	microplane elastic shear modulus
U	recoverable (elastically stored) energy density
V_f	fiber volume fraction
W	work of the stresses
ϵ_{ij}	components of the strain tensor
σ_{ij}	components of the stress tensor
ϵ_N	microplane normal strain
ϵ_M	M -direction shear strain
ϵ_L	L -direction shear strain
ϵ_V	volumetric strain
ϵ_D	deviatoric microplane strain
ϵ_I	maximum principal strain
ϵ_{III}	minimum principal strain
σ_N	microplane normal stress
σ_M	microplane M -direction shear stress
σ_L	microplane L -direction shear stress
σ_{ij}	Kronecker's delta
σ_V^b	boundary value of the volumetric stress
σ_V^0	previous step value of the volumetric stress
σ_D^b	boundary value of the microplane deviatoric stress
σ_N^b	boundary value of the microplane normal stress
σ_N^e	elastic microplane normal stress
σ_T^b	boundary value of the microplane shear stress
σ_f	fiber normal stress
σ_N^{bf}	boundary value of the fiber normal stress
σ_τ	resultant in-plane shear stress
σ_τ^e	elastic resultant in-plane shear stress
σ_τ^b	boundary value of for the in-plane shear stress resultant
σ_M^0	previous step value of the M -direction shear stress
σ_L^0	previous step value of the L -direction shear stress
ν	Poisson's ratio of the model M7f
$\tilde{\nu}$	Poisson's ratio of the parallel coupling model
\mathcal{D}	dissipated energy

Microplane models have a number of advantages. The constitutive model is specified in terms of the stress and strain vectors rather than tensors and their invariants [6]. The principle of frame indifference is still satisfied, albeit approximately, by virtue of using microplanes that sample without bias all possible spatial orientations. The stress and strain vectors are defined on a generic plane within the material microstructure, called the microplane [1], and are related to the macroscopic continuum stress or strain tensor by either a kinematic or a static constraint. The static constraint has been used until today in similar models for hardening plasticity of polycrystalline metals, called Taylor models (proposed by G.I. Taylor in 1938). But in 1984 it was shown that for materials with softening damage the static constraint must be replaced, for reasons of

model stability, by a kinematic constraint and the microplane stress vectors were related to the continuum stress tensor by a variational principle [1,6].

The microplane models are analogous to classical multisurface plasticity but are much simpler because the stress–strain boundaries (representing strain-dependent yield limits) are expressed in terms of vectors rather than tensors. Thanks to this multisurface character, the microplane models can capture: (1) the vertex effect [15], which is major in concrete but is next to impossible to simulate in the tensorial form and also (2) the dilatancy in frictional shear, both without resorting to non-associated plasticity which violates thermodynamic restrictions and causes computational problems [5,15].

M7f introduces several improvements over the previous microplane model M5f for fiber reinforced concrete [10]. One kind of improvement stems from the underlying model M7 for plain concrete. To avoid the spurious lateral expansion and contraction at far postpeak extension, the traditional volumetric–deviatoric split formulation [5] is removed from the elastic strains but is kept for the microplane stress–strain boundaries. The resulting tensile behavior of M7 is similar to model M1 for tensile cracking alone [6]. But in compression the boundaries retain the split, which is necessary to simulate softening and failure in weakly confined compression. Also, M7 can realistically simulate the extensional damage as observed in tensile–compressive loading–unloading and cyclic tests reported in the literature. Furthermore, the observed strong shear dilatancy of low strength concrete [18] can be reproduced by M7. To this end, the volumetric–deviatoric coupling is extended to the volumetric boundary. The aforementioned improvements are made possible by the absence of the elastic volumetric–deviatoric split, which means that the requirement for zero work of the deviatoric (or volumetric) stresses on the volumetric (or deviatoric) strains (postulated in models M4, M5 and M5f) is no longer needed [5,3,4]. As a result, the predictive capabilities of the underlying model M7 have been drastically improved.

The second kind of improvement consists in improved understanding of fiber pullout and breakage, which is as follows. The new effective law for fiber–matrix interaction, along with the well known fiber law for single fibers embedded in a matrix, features three stages, as explained by Fig. 5.

- (1) The first stage is the hardening one, where the stress is transferred to the fibers gradually as a crack forms in the matrix perpendicular to the fibers and all fibers are hardening.
- (2) In the second stage, as the crack opens, the fibers nearest to the crack mouth start pulling out, whereas the fibers away from the crack mouth are still hardening. When the stresses contributed by the uniformly distributed fibers are superposed, according to the parallel coupling model, an approximate plateau with many small oscillations appears, as shown in Fig. 5. The amplitude of these oscillations depends on the fiber volume fraction. For large fractions, this amplitude is small and for small fractions it gets larger.
- (3) The last stage of the fiber constitutive law describes the pull-out of all fibers bridging the crack, which results in overall strain softening. The parallel coupling of fiber bridging and crack opening in the matrix explains the fluctuations observed in the experimental data as well as the variations of the computed ultimate (failure) strain as a function of the fiber volume fraction in fiber reinforced concretes of various kinds.

2. Basic constitutive equations of microplane model M7

Microplane models for concrete are defined using the kinematic constraint, which means that microplane strains are projections of the strain tensor on the microplanes (Fig. 1a) [6,5,3,4]:

$$\epsilon_N = n_i n_j \epsilon_{ij} = N_{ij} \epsilon_{ij} \quad (1)$$

where n_i are the components of the unit normal vector of a generic microplane (Fig. 1b) and $i, j = 1, 2, 3$ are the indices of the cartesian coordinate system. Earlier, similar models, called the slip theory of plasticity or Taylor models, dealt with hardening plasticity of polycrystalline metals and used the static constraint in which the microplane stresses are defined as the projections of the stress tensor onto the microplane. However, in the case of softening damage the static constraint cannot be used since it makes the model unstable [1,6].

The in-plane shear strain vector on each microplane is represented by its two in-plane orthogonal components in the directions of unit in-plane coordinate vectors \vec{m} and \vec{l} which are generated randomly on each microplane. Thus, the shear strains on the microplanes are defined as

$$\epsilon_M = \frac{1}{2} (n_i m_j + n_j m_i) \epsilon_{ij} = M_{ij} \epsilon_{ij}; \quad \epsilon_L = \frac{1}{2} (n_i l_j + n_j l_i) \epsilon_{ij} = L_{ij} \epsilon_{ij} \quad (2)$$

as shown in Fig. 1c.

To capture the differences in damage between tension and compression, it is necessary to split the microplane normal strain and stress into its volumetric and deviatoric parts:

$$\epsilon_N = \epsilon_V + \epsilon_D; \quad \sigma_N = \sigma_V + \sigma_D \quad (3)$$

where $\epsilon_V = \epsilon_{kk}/3$ and $\epsilon_D = (N_{ij} - \delta_{ij}/3) \epsilon_{ij}$. The salient feature of model M7 is that this volumetric–deviatoric split of the normal strain is employed only in the modeling of compressive inelastic behavior, i.e., in the elastic normal strain is not split and all of the tensile behavior is assumed to be governed by the normal strain with no split.

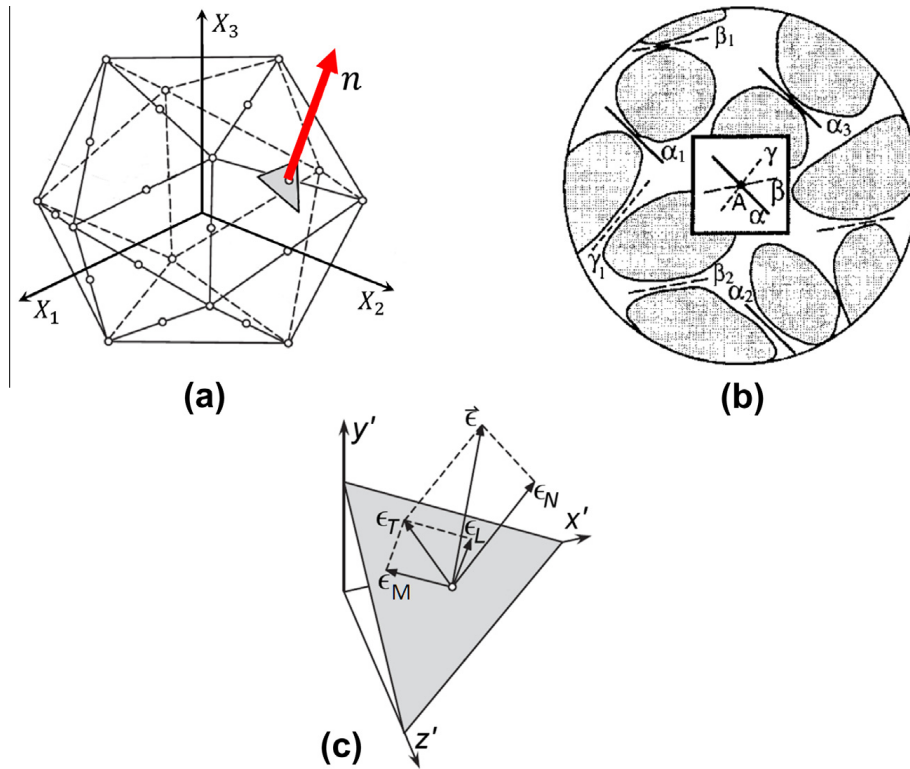


Fig. 1. (a) Example of 21-point optimal Gaussian integration formula (the circled points at the vertices and mid-edges of icosahedron represent the directions of the microplane normals; the optimal weights were calculated in Bažant and Oh 1996). (b) Microplane model ensuing by separate homogenization of slips and openings on weak planes $\alpha_1, \alpha_2, \dots$ of various orientations $\alpha, \beta, \gamma, \dots$ within the representative volume of material. (c) Strain components on the microplane.

To define the constitutive law, the microplane volumetric and deviatoric stresses σ_V and σ_D as well as the microplane shear stresses σ_M and σ_L must be prescribed as functions of the microplane strains. These functions, which must be calibrated by data fitting, are as follows:

$$\sigma_V = \mathcal{F}_V(\epsilon_V, \epsilon_I, \epsilon_{III}); \quad \sigma_D = \mathcal{F}_D(\epsilon_D, \epsilon_V); \quad \sigma_L = \mathcal{F}_T(\epsilon_L, \epsilon_V, \sigma_N); \quad \sigma_M = \mathcal{F}_T(\epsilon_M, \epsilon_V, \sigma_N) \quad (4)$$

Although the constitutive relation for the microplane shear stress components σ_L and σ_M are given in Eq. (4) by the same shear law, this is actually not strictly necessary for ensuring macroscopic isotropy; one may assume an in-plane orthotropy of microplanes and prescribe different shear laws for the two orthogonal shear components on the microplane.

Computationally it is desirable to avoid load step iterations. This means that the microplane constitutive laws should give the microplane stresses explicitly as far as possible. The explicitness has been achieved for the normal stress components on the microplanes. However, the law giving the shear stress components must inevitably be implicit since it must involve the normal stresses, as it is mainly the friction that must be modeled. Likewise, for volume change, a good model must distinguish between pure volumetric (or hydrostatic) compression and uniaxial compression at zero lateral strain, and this requires the volumetric compressive stress to depend on the difference of extreme principal strains.

2.1. Volumetric boundary

The volumetric boundary simulates the pore collapse and expansive breakup of the material (Fig. 4c). It is given by:

$$\sigma_V^b = -Ek_1k_3e^{-\epsilon_V/k_1\alpha} \quad (5)$$

where

$$\alpha = \frac{k_5}{1 + \epsilon_e} \left(\frac{\epsilon_I^o - \epsilon_{III}^o}{k_1} \right)^{c_{20}} + k_4 \quad (6)$$

in which k_i ($i = 1, 2, 3, \dots$) are the adjustable scaling parameters whose numerical values will be discussed later, and $\epsilon_I^o, \epsilon_{III}^o$ are the maximum and minimum principal strains at the beginning of the step and $\epsilon_e = \langle -\sigma_V^o/E_{N0} \rangle$ (where $\langle x \rangle = \max(x, 0)$ = Macauley brackets).

2.2. Deviatoric Boundary

The deviatoric boundary simulates the spreading and splitting cracks under compression (Fig. 4b). It is given by:

$$\sigma_D^b = -\frac{Ek_1\beta_3}{1 + [(-\epsilon_D)/(k_1\beta_2)]^2} \quad (7)$$

where

$$\beta_2 = c_5\gamma_1 + c_7(V_f), \quad \beta_3 = c_6\gamma_1 + c_8, \quad \gamma_0 = f'_{c0}/E_0 - f'_c/E \quad (8)$$

$$\gamma_1 = e^{\gamma_0} \tanh(c_9\langle -\epsilon_V \rangle / k_1) \quad (9)$$

2.3. Normal boundaries

The normal boundaries govern the tensile and compressive fracturing behavior (Fig. 4a). For tensile fracturing

$$\sigma_N^b = Ek_1\beta_1 e^{-(\epsilon_N - \beta_1 c_2 k_1) / (-c_4 \epsilon_e \text{sgn}(\epsilon_e) + k_1 c_3)}$$

where

$$\beta_1 = -c_1 + c_{17} e^{-c_{19}(\epsilon_e - c_{18})} + p_0(V_f) \quad (10)$$

For compressive behavior, the normal boundary is constructed as the sum of volumetric and deviatoric boundaries. For any state of stress, regardless of whether it is tensile or compressive, the normal stress is evaluated using

$$\sigma_N = \max [\min (\sigma_N^e, \sigma_N^b), \sigma_V^b + \sigma_D^b] \quad (11)$$

where σ_N^e is given in Eq. (17) and E_N is given in the first of Eq. (12).

2.4. Elastic behavior, unloading and stiffness degradation

When the normal microplane strains ϵ_N are not split into their volumetric and deviatoric parts, ϵ_V and ϵ_D , with independent elastic constants for each, the normal and shear stiffness constants E_N , E_T on the microplanes under a kinematic constraint are [16, Eq. 32]:

$$E_N = \frac{E}{1 - 2\nu}, \quad E_T = E_N \frac{1 - 4\nu}{1 + \nu} \quad (12)$$

where E = Young's modulus on the macrolevel and ν = Poisson's ratio (also $E_N = K/3$ where K = bulk modulus). Since both E_N and E_T must be nonnegative, only Poisson's ratios in the range $\nu \in [-1, 0.25]$ can be reproduced. This range of ν is sufficient for concrete, for which $\nu \approx 0.18$, but would not suffice for some other materials with $\nu \in (0.25, 0.5]$, such as metals, ceramics, polymers or ice. For those, one easy remedy, mentioned in [6], is to make the microplane model coupled in series with a shear-deformable but incompressible elastic element that is subjected to the same stress tensor σ_{ij} , has an infinite (or very large) bulk modulus \tilde{K} and a finite shear modulus \tilde{G} (Fig. 2). Since, for such a coupled model, the bulk and shear compliances are $\tilde{K}^{-1} = K^{-1}$ and $\tilde{G}^{-1} = G^{-1} + G'^{-1}$, Poisson's ratio is (e.g. [19]):

$$\tilde{\nu} = \frac{3K(1 + G/G') - 2G}{6K(1 + G/G') + 2G} \quad (13)$$

which tends to 0.5 when $G'/G \rightarrow 0$. Any Poisson's ratio, up to 0.5, can thus be reproduced (without a volumetric–deviatoric split). Since the serial element is elastic, all the inelastic behavior and postpeak softening is localized into the microplane model.

Here the coupling of such a serial element is not introduced since it is unnecessary. Nevertheless, $\nu = 0.18$ could also be obtained with such coupling when E_N and E_T are set so as to give less than 0.18 without the coupling. But it seems that the modeling capability would not get enhanced by such coupling, although this is one point that deserves deeper scrutiny (especially for a material with ν less than, but close to, 0.25).

In microplane models M1 and M2, the tangential microplane stiffness was varied as a function of strain. However, beginning with model M3 [9], it appeared simpler to introduce strain-dependent strength (or yield) limits, called the stress–strain boundaries. Within the boundaries, the response is elastic and during the first loading the microplane elastic stiffness E_N and E_T is constant.

Experiments show the pre-and post-peak macrolevel stress–strain curves to vary their slope gradually. This feature is, in microplane simulations with constant E_N and E_T , automatically reproduced by virtue of the fact that the stress–strain boundary is reached at different microplanes at different moments of loading. Similarly, during macroscopic unloading, different microplanes return from the stress–strain boundary into the elastic domain at different moments, which again causes the unloading curves to change unloading slope gradually, with a progressively decreasing slope as the unloading proceeds. Similar comments apply to reloading.

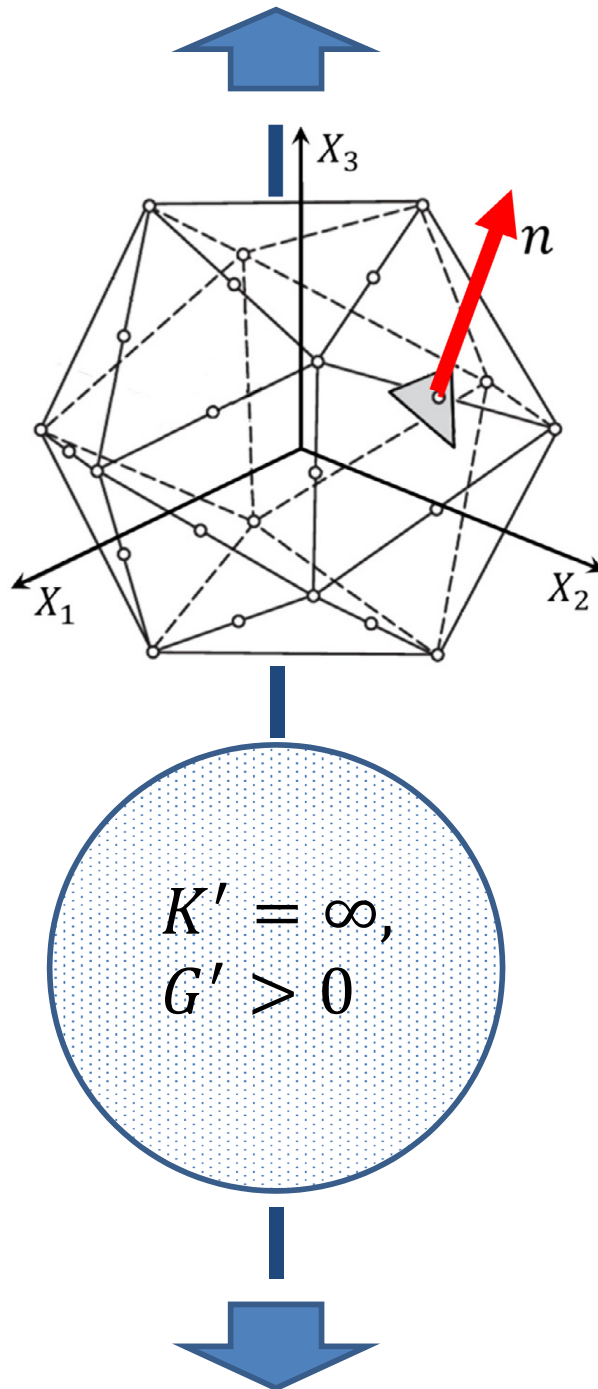


Fig. 2. Any thermodynamically admissible Poisson's ratio can be used if the microplane model is coupled with an elastic element having only bulk modulus (in the present model for concrete, $G' = \infty$, i.e., the coupled element is rigid and the strain in the microplane mode is the total strain).

The normal microplane elastic modulus evolves as follows:

For $\sigma_N^0 \geq 0$:

$$E_N = E_{N0} e^{-c_{13} \epsilon_N^0} f(\zeta) \tag{14}$$

$$\text{but } E_N = E_{N0} \text{ if } \sigma_N^0 > E_{N0} \epsilon_N \text{ and } \sigma_N^0 \Delta \epsilon_N < 0 \tag{15}$$

For $\sigma_N^0 < 0$:

$$E_N = E_{N0} \left(e^{-c_{14} |\epsilon_N^0| / (1+c_{15} \epsilon_e)} + c_{16} \epsilon_e \right) \tag{16}$$

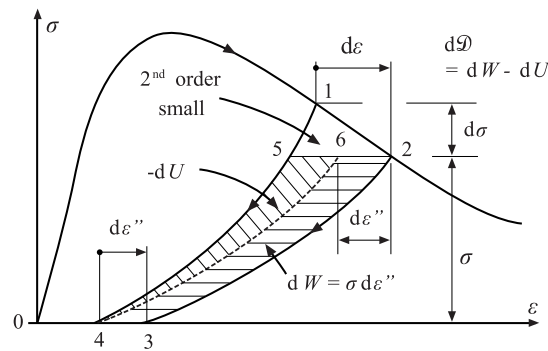


Fig. 3. Dependence of energy dissipation in strain-softening materials on the unloading behavior.

In Eq. (14), $f(\zeta) = (1 + a\zeta^2)^{-1}$ in which $\zeta = f(d\epsilon_V)$ and typically $a = 0.1$ has been employed to extend the validity of the model to many load cycles and has virtually no effect for the first few cycles [21].

The elastic normal microplane stress is given by:

$$\sigma_N^e = \sigma_N^0 + E_N \Delta \epsilon_N \tag{17}$$

When unloading occurs on the microplanes with normals in the direction of the maximum principal tensile strain, the response will inevitably intersect the initial elastic loading path. This is due to the damage (or degradation) of the elastic stiffness. The condition in Eq. (15) makes sure that, after the intersection, the unloading follows the initial elastic slope towards the origin, instead of continuing to proceed along the original unloading path even after the intersection. Following the original unloading path after the two paths have intersected would be incorrect because it would cause negative dissipation during load cycles.

2.5. Frictional Yield Surface

The frictional yield surface simulates the shear behavior of the model (Fig. 4d). It is given by:

$$\sigma_T^b = F_T(-\sigma_N) = \frac{E_T k_1 k_2 (V_f) c_{10} (V_f) \langle -\sigma_N + \sigma_N^0 \rangle}{E_T k_1 k_2 (V_f) + c_{10} (V_f) \langle -\sigma_N + \sigma_N^0 \rangle} \tag{18}$$

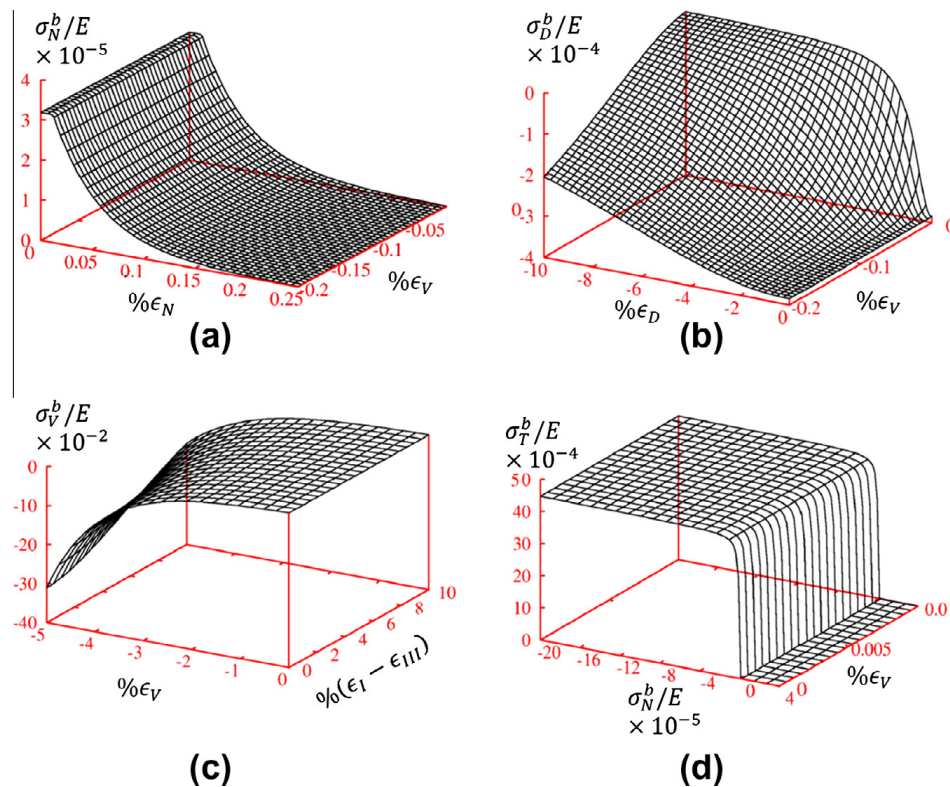


Fig. 4. (a) Normal, (b) deviatoric, (c) volumetric and (d) shear boundaries used for the concrete matrix.

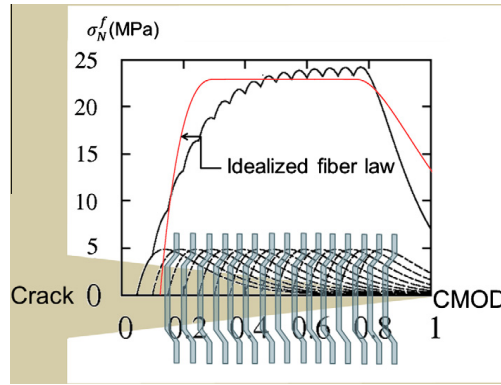


Fig. 5. The overall fiber law used in the modeling of fiber behavior obtained by superposing the responses of individual fibers.

where

$$\sigma_N^0 = \langle E_T k_1 c_{11} (V_f) - c_{12} (V_f) \langle \epsilon_V \rangle \rangle \quad (19)$$

Under compression, the best data fits are obtained when the shear boundary is applied to the microplane shear components before the peak load is reached, especially in fitting the strength envelopes.

2.6. Fiber Constitutive Relation

When the cracks are of the opening mode, the contribution of fiber to the crack bridging stress is given by a simplified form of Kholmyansky's equation [20]:

$$\sigma_N^f = \begin{cases} E p_1 k_1 \langle \epsilon_N / k_1 \rangle e^{-p_2 \langle \epsilon_N / k_1 \rangle} & \text{if } \epsilon_N / k_1 < 1/p_2 + p_4 \\ E p_1 k_1 / p_2 e^{-1} & \text{if } 1/p_2 + p_4 \leq \epsilon_N / k_1 < p_3 \\ E p_1 k_1 \langle \epsilon_N / k_1 - p_3 + 1/p_2 \rangle e^{-p_2 \langle \epsilon_N / k_1 - p_3 + 1/p_2 \rangle} & \text{if } p_3 \leq \epsilon_N / k_1 \end{cases} \quad (20)$$

This law results from gradual activation of fibers bridging an opened crack as shown in Fig. 5. Obviously, the fiber and the matrix are assumed to be coupled in parallel, resulting in a microplane normal stress given by

$$\sigma_N^{bf} = \sigma_N^b + \sigma_N^f \quad (21)$$

where σ_N^{bf} = total normal boundary for fiber reinforced concrete, σ_N^b = boundary for plain concrete matrix and σ_N^f = contribution of the fiber given by Eq. (20).

In the presence of fibers, to calculate the microplane normal stresses σ_N , Eq. (11) is modified by replacing the σ_N^b by σ_N^{bf} :

$$\sigma_N = \max \left[\min \left(\sigma_N^e, \sigma_N^{bf} \right), \sigma_V^b + \sigma_D^b \right] \quad (22)$$

where σ_N^e is given in Eq. (17) and E_N is given in the first of Eq. (12). The microplane shear stresses are obtained by

$$\sigma_\tau = \min \left(|\sigma_\tau^e|, \sigma_\tau^b \right) \quad (23)$$

$$\Delta \sigma_M = E_T \Delta \epsilon_M \frac{\sigma_\tau}{\sigma_\tau^e} \quad (24)$$

$$\Delta \sigma_L = E_T \Delta \epsilon_L \frac{\sigma_\tau}{\sigma_\tau^e} \quad (25)$$

where $\sigma_\tau^e = \sqrt{(\sigma_M^0 + E_T \Delta \epsilon_M)^2 + (\sigma_L^0 + E_T \Delta \epsilon_L)^2}$, $\sigma_M = \sigma_M^0 + \Delta \sigma_M$, $\sigma_L = \sigma_L^0 + \Delta \sigma_L$ and E_T is given by the second of Eq. (12). Finally the micro-macro stress equilibrium is enforced by

$$\sigma_{ij} = \frac{3}{2\pi} \int_{\Omega} [\sigma_N N_{ij} + \sigma_M M_{ij} + \sigma_L L_{ij}] d\Omega \quad (26)$$

2.7. Thermodynamic dissipation

Thermodynamically sound constitutive models must obviously satisfy the condition that the density of dissipation rate must be nonnegative. In microplane models, this criterion could be easily satisfied by requiring the dissipation rate on each microplane to be nonnegative. However, there are two problems with such a simple requirement:

- (1) The dissipation rate on each microplane being nonnegative is only a sufficient condition, not a necessary one; only the dissipation rate on all the microplanes combined must be nonnegative, which means that it can be negative on some.

- (2) Purely elastic unloading is not realistic, and so the effect of damage due to material stiffness loss must be known. Depending on the unloading path, energy can be, and is, dissipated or released.

Is it important to distinguish between sufficient and necessary? It is. Previously [8], an automatic correction in each loading step of a microplane model was developed to satisfy the dissipation criterion on each microplane separately. But such a correction was subsequently found to be far too stringent, making it impossible to fit most test data.

The density of energy dissipation increment may be written as $dD = dW - dU$ where $dW = \sigma_{ij}d\epsilon_{ij}$ = work of stress on the strain increments, and U = density of recoverable stored energy. Unfortunately, the value of U , as affected by material damage (a damage that can continue during unloading) is in general very difficult to determine.

To illustrate the difficulty, consider [similar to] [8] one stress and one strain component only, and a general stress–strain diagram with strain softening, $\sigma(\epsilon)$, as shown in Fig. 3. An infinitesimal strain increment $d\epsilon$ from point 1 to point 2 leads to continuing material damage which causes the unloading path to change from curve $\bar{1}4$ to curve $\bar{2}3$. Curve $\bar{6}4$ is a rigid-body shift of $\bar{2}3$ to the left. Since $d\epsilon$ is infinitesimal, $\bar{5}1$ is also infinitesimal. So the work given by the triangle $\bar{1}25\bar{1}$ is second-order small, infinitely smaller than the cross-hatched areas, and thus negligible. The increment of dissipated work dW is represented by area $\bar{2}346\bar{2}$, and the decrement of stored energy, $dU (<0)$, or the energy dissipation due to damage, by area $\bar{4}564$. So, in this one-component setting, a sufficient requirement of nonnegative energy dissipation is that the combined (cross-hatched) area $\bar{2}345\bar{2}$ be nonnegative. But this is not a necessary requirement. Only the sum of all the areas of the type $\bar{2}345\bar{2}$ over all the stress components must be nonnegative.

In microplane models, negativeness of the areas of the type $\bar{2}345\bar{2}$ on some microplanes is admissible if their sum over all the microplanes is nonnegative. This is one difficulty. Another is that a realistic check for nonnegative dissipation must include multi-axial stress paths, such as a closed loop consisting of normal stress increment, shear stress increment, normal stress decrement and shear stress decrement returning to the original zero stress tensor.

An example of such a loop was given in Carol et al. [17] for microplane model M2, with the conclusion that energy dissipation could be negative. However, the unloading path was considered to be a straight line always pointed to the origin, which is unrealistic and is not the way model M2 has been used. If the unloading is assumed to follow a constant elastic stiffness, no problem occurs for M2.

For the present model M7, computations have been run for some similar closed loops and no negative dissipation has been found. But a general analytical dissipation check of M7, covering all the possible loops, seems difficult.

3. Calibration and data fits

The optimum numerical simulations of the experimental data for concretes reinforced with Harex, PVA and Dramix fibers subjected to uniaxial tension are shown in Figs. 6–8 [23], and those with Dramix fibers in Figs. 9–11 [22]. The simulation for steel fiber reinforced concretes under uniaxial and triaxial compression are presented in Fig. 12 and Figs. 14–17 [18] respectively. The volumetric compression test data and their simulations are depicted in Fig. 13 [18]. The agreement of the simulations with the data is seen to be quite satisfactory.

The free and fixed parameters of the model for concrete matrix, their values and their brief descriptions, are given in Tables 5 and 6. The “c” parameters are the fixed parameters, which do not change from one concrete to another; the “k” parameters may change from one concrete to another and thus they must be calibrated for each given concrete. Although there seem to be too many parameters, only five of them are free parameters for the concrete matrix (k_1, \dots, k_5). There are five more free parameters (p_0, \dots, p_4), which must be supplied by the user. They characterize the fiber effect on the opening, splitting and slipping type fracture.

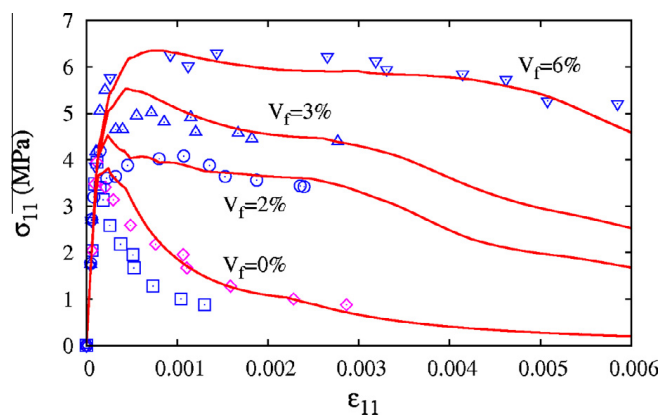


Fig. 6. Uniaxial tensile test data for FRC with $V_f = 2\%$, 3% and 6% of Harex fibers [23] and their simulation by the model M7f. The data for plain concrete under uniaxial tension is also shown for comparison.

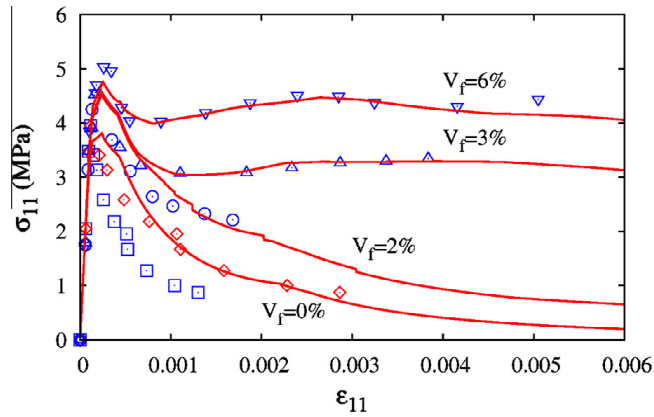


Fig. 7. Uniaxial tensile test data for FRC with $V_f = 2\%$, 3% and 6% of PVA fibers [23] and their simulation by the model M7f. The data for plain concrete under uniaxial tension is also shown for comparison.

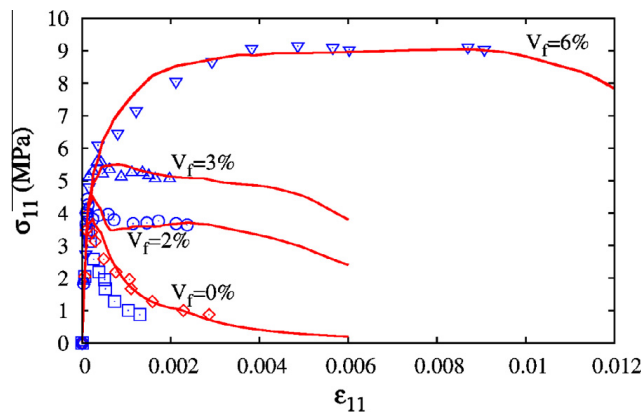


Fig. 8. Uniaxial tensile test data for FRC with $V_f = 2\%$, 3% and 6% of Dramix fibers [23] and their simulation by the model M7f. The data for plain concrete under uniaxial tension is also shown for comparison.

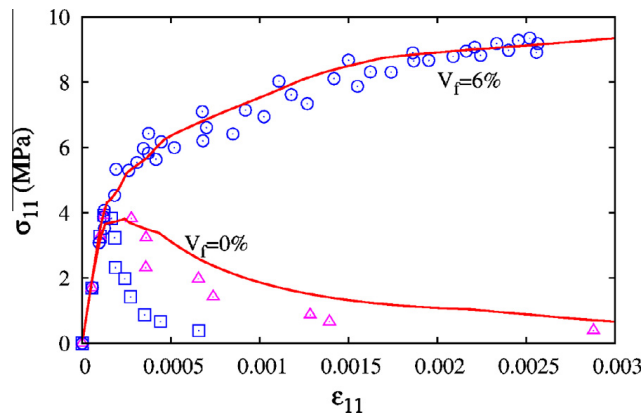


Fig. 9. Uniaxial tensile test data for FRC with $V_f = 6\%$ of Dramix fibers [22] and its simulation by the model M7f. The data for plain concrete under uniaxial tension is also shown for comparison.

For most low and normal strength concretes, the values provided in Tables 5 and 6 should be sufficient for calibration of the concrete matrix behavior. For others, the free parameters, (k_1, \dots, k_5) need to be identified from the test data obtained on specimens of the concrete under consideration. For various types of fibers, the values of free fiber parameters (p_0, \dots, p_4) are already determined as shown in Tables 1a–c, 2–4. But if a new type of fiber is used, these values must be recalibrated. This can be done by fitting the test data on uniaxial tension and uniaxial compression.

In the comparisons of the available experimental results with the numerical fits achieved, presented in Figs. 6–18, the experimental data are shown by symbols and the simulations are shown by continuous lines. Each diagram in the figures

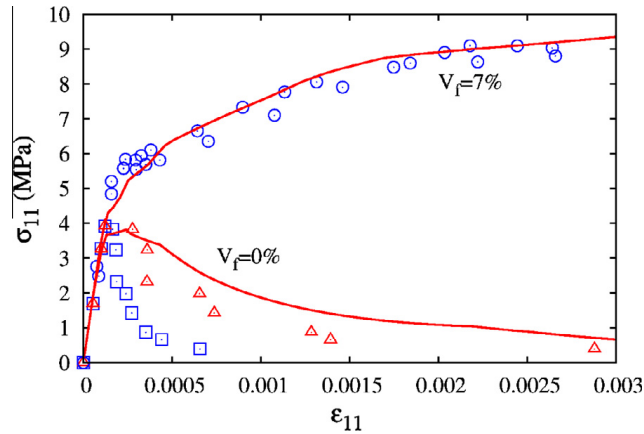


Fig. 10. Uniaxial tensile test data for FRC with $V_f = 7\%$ of Dramix fibers [22] and its simulation by the model M7f. The data for plain concrete under uniaxial tension is also shown for comparison.

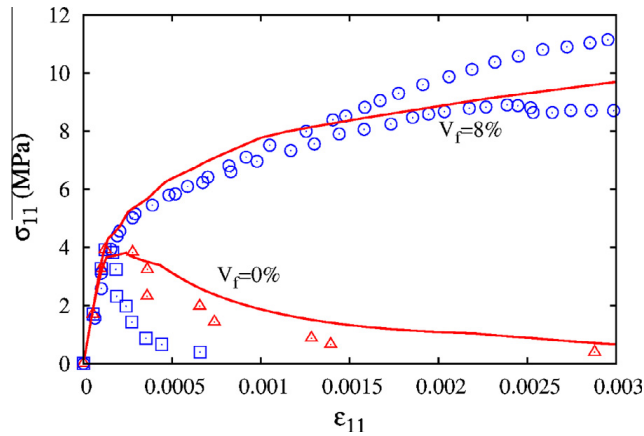


Fig. 11. Uniaxial tensile test data for FRC with $V_f = 8\%$ of Dramix fibers [22] and its simulation by the model M7f. The data for plain concrete under uniaxial tension is also shown for comparison.

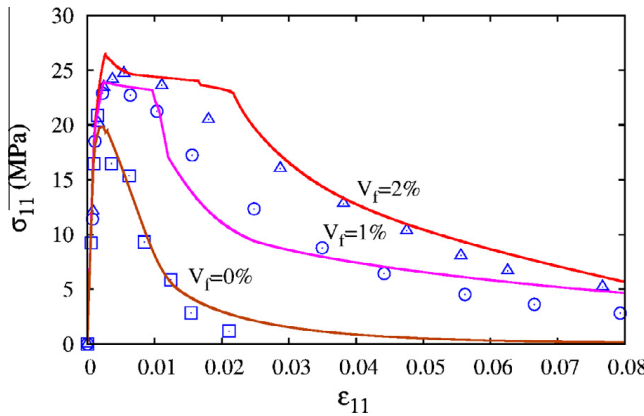


Fig. 12. Uniaxial compression test data for FRC with $V_f = 0\%$, 1% and 2% of carbon steel fibers [18] and their simulation by the model M7f.

is plotted in terms of the average stress and average strain in the test specimen. All the simulations were made using the 37-point Gaussian numerical integration formula for a unit hemisphere [7], which integrates exactly a polynomial of the 13th degree.

Figs. 6–8 show the data and optimum fits for the uniaxial tensile tests reported in [23] and conducted on concretes with $V_f = 0\%$, 2%, 3%, and 6%. Three different types of reinforcement were used: (1) steel fibers “Dramix” (diameter 0.5 mm, length 30 mm, hooked ends); (2) steel fibers “Harex” (having an arched cross section of dimensions 2.20–0.25 mm and the length of

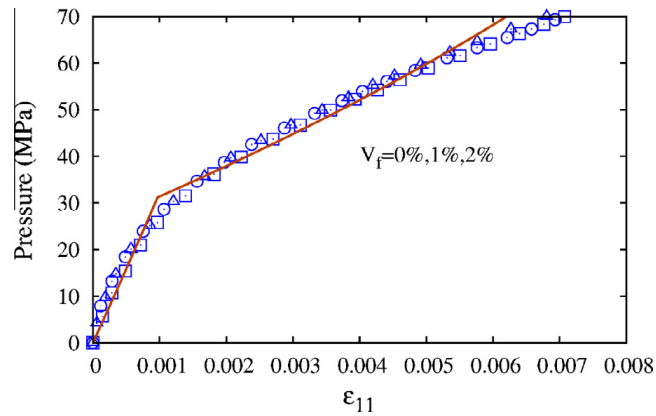


Fig. 13. Hydrostatic compression test data for FRC with $V_f = 0\%$, 1% and 2% of carbon steel fibers [18] and their simulation by the model M7f.

Table 1
Fiber parameters for Figs. 6–8.

V_f	0%	2%	3%	6%
(a)				
p_0	0	0.0165	0.0346	0.125
p_1	0	0.4	0.45	0.525
p_2	0.3	0.264	0.214	0.165
p_3	0	21	21	31
p_4	4.5	3	1	1
c_7	100	1000	2000	2000
k_2	100	120	120	120
c_{11}	1	6	7	8
c_{12}	7000	70	7	7
c_{10}	0.33	0.43	0.43	0.43
0%				
(b)				
0		0.0165	0.0346	0.125
0		0.1	0.1	0.225
0.3		0.264	0.1	0.1
0		1	31	41
4.5		4	4	3
100		1000	2000	2000
100		120	120	120
1		6	7	8
7000		70	7	7
0.33		0.43	0.43	0.43
(c)				
0		0.0165	0.0346	0.125
0		0.3	0.45	0.55
0.3		0.175	0.175	0.1
0		31	31	71
4.5		4	1.25	1.25
100		1000	2000	2000
100		120	120	120
1		6	7	8
7000		70	7	7
0.33		0.43	0.43	0.43

32 mm); and (3) synthetic fibers made of polyvinyl alcohol (PVA) (diameter 0.66 mm, length 30 mm). Figs. 9–11 show the data and fits for the uniaxial tensile tests reported in [22] and conducted on concretes reinforced by Dramix fibers, with three tests for $V_f = 6\%$, two for 7% , and two for 8% . In Figs. 6–11, for uniaxial tension response of plain concrete two sets of data points are shown. The squares are for the original experimental data and diamonds are for the delocalized data [9].

The optimal parameters are identified starting with the concrete matrix, which is characterized by E , ν and the adjustable parameters of model M7. For the diagrams in Figs. 6–8, the values $E = 35$ GPa, $\nu = 0.18$, $k_1 = 0.000120$, $k_2 = 100$, $k_3 = 20$, $k_4 = 40$, $k_5 = 0.0001$ are obtained for the concrete matrix. The fiber parameters are given in Table 1a–c. For the diagrams in Figs. 9–11

Table 2
Fiber parameters for Figs. 9–11.

V_f	0%	6%	7%	8%
p_0	0	0.125	0.125	0.125
p_1	0	0.55	0.55	0.55
p_2	0.3	0.09	0.09	0.085
p_3	0	71	71	71
p_4	4.5	1.25	1.25	1.25
c_7	100	2000	2000	2000
k_2	100	120	120	120
c_{11}	1	8	8	8
c_{12}	7000	7	7	7
c_{10}	0.33	0.43	0.43	0.43

Table 3
Fiber parameters for Figs. 12–17.

V_f	0%	1%	2%
p_0	0	0.0083	0.0165
p_1	0	0.178	0.357
p_2	0.3	0.266	0.234
p_3	0	4.22	5.09
p_4	4.5	3.75	3
c_7	100	1000	1000
k_2	100	110	120
c_{11}	1	3	6
c_{12}	7000	700	70
c_{10}	0.33	0.43	0.43

Table 4
Fiber parameters for Fig. 18.

V_f	0%	1%	2%
p_0	0	0.0083	0.0165
p_1	0	0.2	0.4
p_2	0.3	0.282	0.264
p_3	0	10.5	21
p_4	4.5	3.75	3
c_7	100	1000	1000
k_2	100	110	120
c_{11}	1	3	6
c_{12}	7000	700	70
c_{10}	0.33	0.43	0.43

Table 5
Free parameters of model M7, their typical (or default) values and their meanings.

Parameter	Value	Meaning
E	25,000 MPa	Elastic modulus, (and vertical scaling parameter)
ν	0.18	Poisson's ratio
k_1	1.5×10^{-4}	Radial scaling parameter
k_2	110	Controls the horizontal asymptote value in the frictional boundary
k_3	30	Controls the shape of the volumetric boundary
k_4	100	Controls the shape of the volumetric boundary
k_5	1×10^{-4}	Controls the volumetric–deviatoric coupling at low pressures

the parameters differing from the foregoing ones are shown in Table 2. The fiber effect is subsequently calibrated by adjusting parameters p_0, \dots, p_4 .

The experimental data in Figs. 12–17 were reported in [18] and were obtained on fiber-reinforced concretes with carbon steel fibers of $V_f = 0\%$, 1%, and 2%. The specimens are loaded in multiaxial compression, in a kinematically constrained system. The concrete matrix properties are: $E = 20$ GPa, $\nu = 0.18$, $k_1 = 0.000090$, $k_2 = 100$, $k_3 = 6$, $k_4 = 60$, $k_5 = 0.0001$. In general, the fiber effect on the compressive triaxial response of the material is significant for a concrete matrix of relatively lower strength, as is the case for the material corresponding to Figs. 12–17.

Table 6
Fixed parameters of the model M7, their typical values and their meanings.

Parameter	Value	Meaning
f_{c0}^f	15.08 MPa	Reference compressive strength
E_0	20GPa	Reference elastic modulus
c_1	8.9×10^{-2}	Controls the uniaxial tensile strength
c_2	17.6×10^{-2}	Controls the roundness of the peak in uniaxial tension
c_3	4	Controls the slope of the postpeak in uniaxial tension
c_4	50	Controls the slope of the postpeak tail in uniaxial compression
c_5	3500	Controls the vol. expansion under compression
c_6	20	Controls the roundness of the peak in vol. expansion under compression
c_7	1	Controls the slope of the initial postpeak in uniaxial compression
c_8	8	Controls the peak strength in uniaxial compression
c_9	1.2×10^{-2}	controls the peak roundness in uniaxial compression
c_{10}	0.33	Controls the effective friction coefficient
c_{11}	0.5	Initial cohesion in frictional response
c_{12}	2.36	Controls the change of cohesion with tensile vol. strains
c_{13}	4500	Controls the unloading slope in tension
c_{14}	300	Controls the unloading slope at low hydrostatic compression
c_{15}	4000	Controls the transition from unloading slope at high confinement to that at low confinement
c_{16}	60	Controls the unloading slope at high hydrostatic compression
c_{17}	1.4	Controls the tensile strength
c_{18}	1.6×10^{-3}	Controls the tensile cracking under compression
c_{19}	1000	Controls the tensile softening rate induced by compression
c_{20}	1.8	Controls the volumetric–deviatoric coupling at high pressures

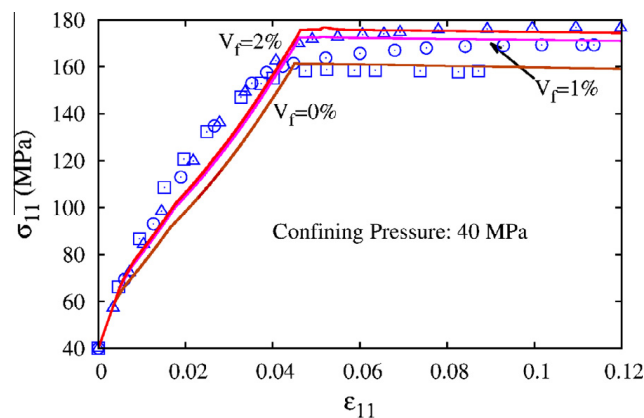


Fig. 14. Triaxial compression test data at a confining pressure of 40 MPa for FRC with $V_f = 0\%$, 1% and 2% of carbon steel fibers [18] and their simulation by the model M7f.

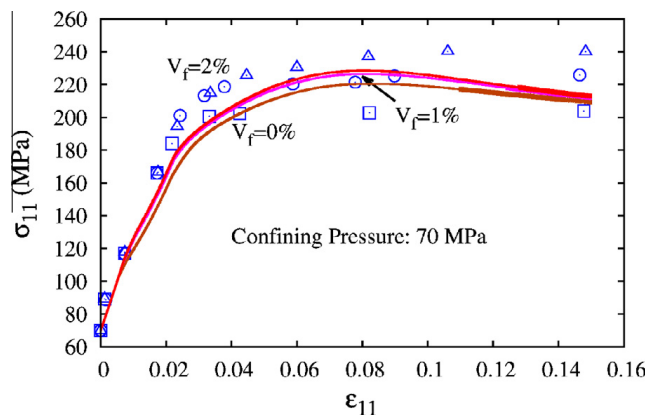


Fig. 15. Triaxial compression test data at a confining pressure of 70 MPa for FRC with $V_f = 0\%$, 1% and 2% of carbon steel fibers [18] and their simulation by the model M7f.

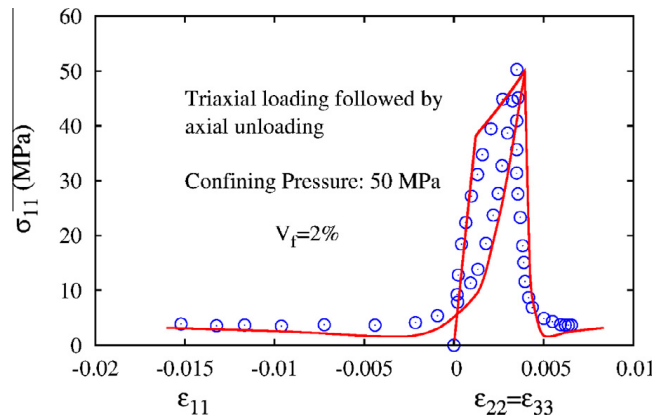


Fig. 16. Triaxial compression test data with unloading at a confining pressure of 50 MPa for FRC with $V_f = 2\%$ of carbon steel fibers [18] and its simulation by the model M7f.

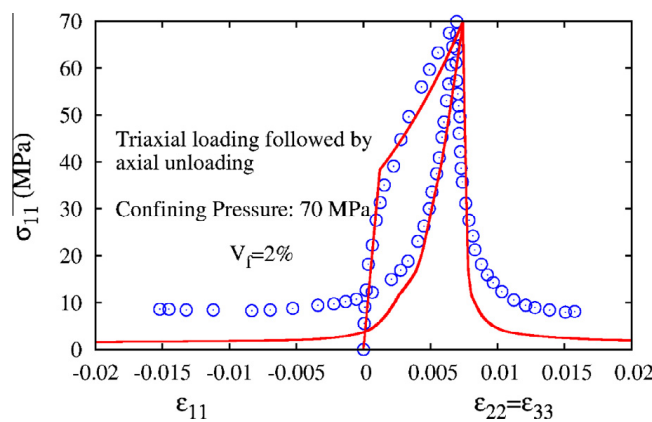


Fig. 17. Triaxial compression test data with unloading at a confining pressure of 70 MPa for FRC with $V_f = 2\%$ of carbon steel fibers [18] and its simulation by the model M7f.

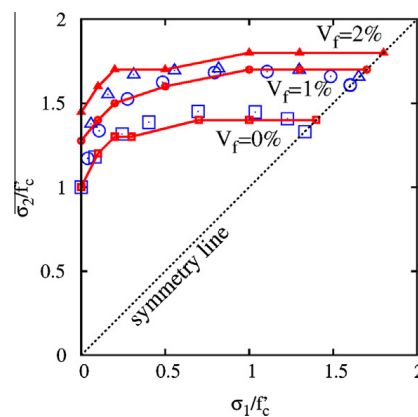


Fig. 18. Biaxial compression test data for FRC with $V_f = 0\%$, 1% and 2% of steel fibers [24] and their simulation by the model M7f.

To model the fiber volume effects, one parameter of the compressive deviatoric boundary, c_7 , and parameters k_2 , c_{10} , c_{11} and c_{12} of the friction boundary, have been generalized to be functions of V_f . The values of these parameters are given in Table 3. For hydrostatic compression (Fig. 13), the fiber reinforced concrete exhibits no significant differences from normal concrete (at least for $V_f \leq 2\%$). The triaxial compression tests in Figs. 14 and 15 are used to calibrate the parameters dependent on the fiber volume fraction, given in Table 3.

Fig. 18 shows the test results for biaxial compression of steel fiber reinforced concrete with $V_f = 0\%$, 1% , and 2% , as reported in [24]. The concrete matrix in the numerical simulations is characterized by: $E = 20$ GPa, $\nu = 0.18$, $k_1 = 0.000140$, $k_2 = 100$,

$k_3 = 13$, $k_4 = 70$, $k_5 = 0.0001$ MPa. The optimized values for $V_f = 0\%$, 1% , and 2% of the fiber parameters are given in Table 4. These parameters have been identified to match the mean overall failure envelope.

Finally, Figs. 16 and 17 show a fit of a hydrostatic compression test followed by unloading. The simulations for both axial and transverse deformations are seen to closely follow the test results.

As seen, the foregoing simulations generally attain satisfactory agreement with the experimental data. This confirms the soundness of the present model. In Fig. 18, the biaxial compression failure envelope shows only small discrepancies with the experiments in the proportional loading direction, which is observed in model M7 for plain concrete as well.

Addition of several new parameters to those already involved in model M7 might be suspected of making model M7f too difficult to calibrate. Not so, however, because the model parameters need not be optimized by simultaneous fitting of all the test data, and because the new parameters in M7f have a clear and easily identifiable trend with respect to V_f . The following sequential calibration procedure, in which only a few parameters are optimized to fit only one simple type of test, is simple to carry out.

1. Identify the parameters of model M7 considering only concrete without fibers.
2. From the uniaxial tension data, identify $p_0(V_f)$, $p_1(V_f)$, $p_2(V_f)$, $p_3(V_f)$ and $p_4(V_f)$. Parameter $p_0(V_f)$ decides whether the fibers engage as soon as the fracturing localizes in the concrete matrix. Parameter $p_1(V_f)$ controls the vertical scaling of fiber contribution, and $p_2(V_f)$ controls the pull-out of fibers that bridge an opening crack. Parameters $p_3(V_f)$ and $p_4(V_f)$ determine the length of the plastic plateau in the microplane stress–strain diagram of the fibers.
3. From the uniaxial compression data, identify $c_7(V_f)$ and $c_{12}(V_f)$.
4. From the triaxial compression data, identify $k_2(V_f)$, $c_{10}(V_f)$, and $c_{11}(V_f)$.

The calibration of the free matrix parameters $k_1 \dots k_5$ can easily be made sequentially, with simultaneous optimization of no more than two parameters (for details see [11,3,4,13,14]).

Another application of M7f is the prediction of stress–strain curves for V_f values different from those tested experimentally. This is achieved by interpolating the values of model parameters identified from tests for several different V_f values. By fitting these parameter values, one can identify simple expressions for the functions $p_0(V_f), \dots, p_4(V_f)$ and $k_2(V_f), c_7(V_f), c_{10}(V_f), c_{11}(V_f), c_{12}(V_f)$, etc. Still another application is to predict approximate stress–strain curves for multiaxial loading when only uniaxial test data are available.

4. Conclusions

The present model M7f has two kinds of advantages over its predecessors: (1) It is built on M7, a greatly improved microplane model for plain concrete and (2) the effect of the fibers is captured more realistically than in previous versions, particularly [10].

The advantages of M7, which now transcends to M7f, are, briefly, as follows: (1) The volumetric–deviatoric split is avoided for elastic strains and is applied only to the stress–strain boundaries; (2) As a consequence, the excessive lateral strains and stress locking in far post-peak extension are eliminated and it becomes possible to reproduce differences between hydrostatic compression and uniaxial compression under rigid lateral confinement, as well as the high shear dilatancy of low strength concretes; and (3) the unloading, reloading and load cycles can be captured realistically, even if they cross between tension and compression; in detail, see [13,14].

The effect of fibers is made dependent on the fiber volume fraction and the plain concrete model is recovered when this fraction vanishes. The fiber resistance is a function of the strain representing the average opening of cracks of given spacing. Compared to previous models, introduced is a new refined model in which the fibers bridging the crack and resisting its opening are considered to be in different regimes, some fibers already softening, others still hardening (Fig. 5). A fiber law of the same form is systematically used to fit all the test data, but its parameters vary, depending on the fiber volume fraction and the fiber type.

The resulting model, M7f, is robust, i.e., always works. Robustness is not automatic in the models that can fit a wide range of inelastic behavior. The previous versions M5f and M6f [12] were abandoned due to robustness issues which appeared in large-scale finite element analyses. Here the robustness is achieved by a systematically explicit formulation, i.e., an explicit calculation of stress from strain or deformation in both the concrete matrix and the fibers. Unlike M5f and M6f, neither complex transitions from one kind of formulation to another nor separations of field variables into elastic and inelastic parts are introduced.

Acknowledgments

The early stage of this work was supported by Grant W911NF-09-1-0043 from the US Army Research Office, Durham, to Northwestern University. The final stage was supported by the US Department of Transportation through grant 20778 from the Infrastructure Technology Institute of Northwestern University, and by the Agency for Defense Development (ADD), Korea, through a grant from Daejeon University to Northwestern University.

References

- [1] Bažant Z. Microplane model for strain-controlled inelastic behavior. In: Desai CS, Gallagher RH, editors. J. Wiley, London, 1984. p. 45–59. [chapter 3].
- [2] Bažant ZP. Can multiscale–multiphysics methods predict softening damage and structural failure? *Int J Multiscale Comput Engng* 2010;8(1):61–7 [adapted republication from newsletter *Mechanics* (Am. Academy of Mechanics) 36, 2007, no. 5–6, May–June, 5–12].
- [3] Bažant ZP, Caner FC. Microplane model M5 with kinematic and static constraints for concrete fracture and anelasticity. I. Theory. *J Engng Mech ASCE* 2005;131(1):31–40.
- [4] Bažant ZP, Caner FC. Microplane model M5 with kinematic and static constraints for concrete fracture and anelasticity. II. Computation. *J Engng Mech ASCE* 2005;131(1):41–7.
- [5] Bažant ZP, Caner FC, Carol I, Adley MD, Akers SA. Microplane model M4 for concrete: I. Formulation with work-conjugate deviatoric stress. *J Engng Mech, ASCE* 2000;126(9):944–53.
- [6] Bažant ZP, Oh B-H. Microplane model for progressive fracture of concrete and rock. *J Engng Mech, ASCE* 1985;111:559–82.
- [7] Bažant ZP, Oh B-H. Efficient numerical integration on the surface of a sphere. *Zeitschrift für angewandte Mathematik und Mechanik* 1986;66(1):37–49 [zAMM, Berlin].
- [8] Z.P. Bažant, J.-Y. Wu, F.C. Caner, G. Cusatis, How to enforce non-negative energy dissipation in microplane and other constitutive models of softening damage, plasticity and friction, in: et N.B. al., (Ed.), *Computational Modeling of Concrete structures*, EURO-C Conference. Taylor & Francis, London, Schladming/Rohrmoos, Austria, 2010, pp. 87–91.
- [9] Bažant ZP, Xiang Y, Prat PC. Microplane model for concrete. I. Stress–strain boundaries and finite strain. *J Engng Mech, ASCE* 1996;122(3):245–54.
- [10] Beghini A, Bažant ZP, Zhou Y, Gouirand O, Caner FC. Microplane model M5f for multiaxial behavior and fracture of fiber-reinforced concrete. *ASCE J Engng Mech* 2007;133(1):66–75.
- [11] Caner FC, Bažant ZP. Microplane model M4 for concrete: II. Algorithm and calibration. *J Engng Mech, ASCE* 2000;126(9):954–61.
- [12] Caner FC, Bažant ZP. Microplane model M6f for fiber reinforced concrete. In: Oñate E, Owen DRJ, Suárez DP, B, editors. XI International Conference on Computational Plasticity Fundamentals and Applications, COMPLAS 2011. Barcelona (Spain): CIMNE/UPC, CIMNE; 7–9 September 2011. p. 796–807.
- [13] Caner FC, Bažant ZP. Microplane model M7 for plain concrete: I. Formulation. *J. Engng Mech, ASCE* 2013. [http://dx.doi.org/10.1061/\(ASCE\)JEM.1943-7889.0000570](http://dx.doi.org/10.1061/(ASCE)JEM.1943-7889.0000570).
- [14] Caner FC, Bažant ZP. Microplane model M7 for plain concrete: II. Calibration and verification. *J. Engng Mech, ASCE* 2013;12. [http://dx.doi.org/10.1061/\(ASCE\)JEM.1943-7889.0000571](http://dx.doi.org/10.1061/(ASCE)JEM.1943-7889.0000571).
- [15] Caner FC, Bažant ZP, Červenka J. Vertex effect in strain-softening concrete at rotating principal axes. *J Engng Mech, ASCE* 2002;128(1):24–33.
- [16] Carol I, Bažant ZP. Damage and plasticity in microplane theory. *Int J Solids Struct* 1997;34(29):3807–35.
- [17] Carol I, Jirásek M, Bažant ZP. A thermodynamically consistent approach to microplane theory. Part I: Free energy and consistent microplane stresses. *Int J Solids Struct* 2001;38(17):2921–31.
- [18] Chern J-C, Yang H-J, Chen H-W. Behavior of steel fiber-reinforced concrete in multiaxial loading. *ACI Mater J* 1992;89(1):32–40.
- [19] Fung YC. *Foundations of solid mechanics*. Englewood Cliffs (NJ): Prentice-Hall; 1968.
- [20] Kholmyansky MM. Mechanical resistance of steel fiber reinforced concrete to axial load. *J Mater Civil Engng* 2002;144:311–9.
- [21] Kirane K, Bažant ZP. Modification of the normal boundary in microplane model M7 to simulate Paris Law type fatigue. Private communication; 2013
- [22] Li F, Li Z. Continuum damage mechanics based modeling of fiber-reinforced concrete in tension. *Int J Solids Struct* 2001;38:777–93.
- [23] Li Z, Li F, Chang T-Y-P, Mai Y-W. Uniaxial tensile behavior of concrete reinforced with randomly distributed short fibers. *ACI Mater J* 1998;95(5):564–74.
- [24] Yin WS, Su ECM, Mansur MA, Hsu TTC. Biaxial tests of plain and fiber concrete. *ACI Mater J* 1989;86(3):236–43.